Monografías Matemáticas *García de Galdeano* **40**, 95–104 (2015)

DISCONTINUOUS GALERKIN METHOD APPLIED TO PHOTOTHERMAL INSPECTION OF CRACKED MATERIALS

Ángel Javier Omella and Ricardo Celorrio

Abstract.

In this work we present a generalization of Baumann-Oden-type Discontinuous Galerkin Finite Element Method (DGFEM) to model the thermal wave scattering in lock-in thermographic and vibrothermographic inspection of cracked samples of homogeneous materials. The modelization is based on considering thin cracks as interfaces characterized by its thermal contact resistance.

We check numerically the order of convergence of the method for the 1D case. We present a 3D heat flow numerical simulation of a cracked gear that has been implemented by using a collection of scientific open-source software as an application example.

Keywords: Discontinuous Galerkin, lock-in thermography, crack detection.

AMS classification: 80M10.

§1. Introduction

The detection and characterization of cracks in materials using Non-Destructive Testing (NDT) methods are important tools to prevent the structural failure of components (cf. [9]). In particular, the use of infrared thermographic techniques for this proposal are becoming popular in the last years (cf. [10] [14] [15] [16]). This techniques have demonstrated the ability to detect small cracks although an efficient quantitative analysis for crack characterization is currently being studied.

In the second section of this work we show a model that can be straightforward applied to infrared lock-in thermographic inspection (LT) and infrared lock-in vibrothermographic inspection (LVT) of homogeneous and isotropic materials (cf. [2]). In LT the surface of the sample is illuminated by an optical external source such as a modulated and defocused laser spot that produces a time-harmonic thermal waves into the sample. On the other hand, time-harmonic thermal waves in LVT are produced by the mechanical dissipated heat at the defect due to the excitation of an ultrasonic wave applied to the sample. In both methods the temperature field, amplitude and phase, at the surface of the sample is recorded with an infrared camera.

The application of traditional continuous Finite Element Methods (FEM) (cf. [8]) to cracked samples requires meshing the air located into the gap of the crack, which causes a dramatically increasing of the number of elements in the mesh needed to solve the temperature field. To overcome this problem, we have developed in section 3 a much more efficient numerical method based on Discontinuous Galerkin (DG) elements where thin cracks are considered as interfaces characterized by its thermal contact resistance.

The numerical model that we present is a Baumann-Oden-type Discontinuous Galerkin Finite Element Method (DGFEM) and is an improvement to the method introduced in (cf. [4]) and an extension one of the method considered in (cf. [5]), where the LVT case was not included. Furthermore, in this work we focus on some mathematical aspects about the deduction of the method following the methodology exposed by Douglas *et al.* in (cf. [1]).

In section 4 we check numerically the order of convergence of the method for a 1D case. Finally, in section 5 we show a photothermal application example where a 3D heat flow for LT of a cracked gear of AISI E9310 steel is simulated.

§2. Modelization

Let $\Omega \subset \mathbb{R}^3$ be a bounded open domain (see Figure 1 -left) which models an homogeneous and isotropic material with thermal conductivity κ and thermal diffusivity α. We consider an air-crack placed in the interface $\Gamma_c \subset \Omega$, characterized by its thermal contact resistance $R : \Gamma_c \to \mathbb{R}_{\geq 0}$, being $R\kappa_{air}$ the effective thickness of the crack, where κ_{air} is the conductivity of the air.

In order to present properly the problem, we need to introduce some trace operators, the *average* $\{\cdot\}$ and the *jump* $[\![\cdot]\!]$, defined on any interior interface Γ definable into the domain Ω (as for example Γ_c). Let us define the outward normal vectors to each side of the interface $\boldsymbol{n}_+$ and $\boldsymbol{n}_-$, where subscripts + and − denote right and left sides respectively (from the point of view of an arbitrary observer sited in the interface); the trace operator are

$$\{\cdot\} := \frac{(\cdot)^+ + (\cdot)^-}{2}, \quad [\![\cdot]\!] = (\cdot)^+\boldsymbol{n}_+ + (\cdot)^-\boldsymbol{n}_-, \quad \text{for any interface } \Gamma \in \Omega.$$

The spacial component $u : \Omega \to \mathbb{C}$ of the thermal wave at frequency $\nu > 0$, $\Re\left(u(\boldsymbol{x})\mathrm{e}^{-i2\pi\nu t}\right)$, induced into Ω is governed by the following discontinuous transmission problem:

$$\Delta u + i\frac{2\pi\nu}{\alpha}u = 0, \qquad \text{in } \Omega \setminus \Gamma_c, \tag{1a}$$

$$\kappa[\![\nabla u]\!]\Big|_{\Gamma_c} = f_1, \qquad \text{on } \Gamma_c, \tag{1b}$$

$$[\![u]\!]\Big|_{\Gamma_c} + R\kappa\{(\nabla u, \cdot\boldsymbol{n})\boldsymbol{n}\}\Big|_{\Gamma_c} = \boldsymbol{f_2} \qquad \text{on } \Gamma_c, \tag{1c}$$

$$\kappa\nabla u \cdot \boldsymbol{n}\Big|_{\partial\Omega} = g, \qquad \text{on } \partial\Omega; \tag{1d}$$

where the spatial components of the ν-harmonic thermal sources exciting the material are: two heat sources $f_1 : \Gamma_c \to \mathbb{C}$ in the flux continuity equation (1b) and $g : \partial\Omega \to \mathbb{C}$ in the boundary condition (1d); and a temperature source $\boldsymbol{f_2}(\boldsymbol{x}) := f_2(\boldsymbol{x})\boldsymbol{n}^+(\boldsymbol{x})$, being $f_2 : \Gamma_c \to \mathbb{C}$ a complex-valued function, in the discontinuity transmission condition (equation 1c). The heat source f_1 is related to vibrothermographic inspections and g to the heat transmitted by the illumination of the surface in photothermal techniques.

The discontinuous transmission condition (1c) requires a constrain on the space $H^1(\Omega\setminus\Gamma_c)$ in the standard variational formulation (similar to the discrete version in (11)) of (1), being the space of admissible functions $V := \left\{v \in H^1(\Omega \setminus \Gamma_c \to \mathbb{C}) \;\middle|\; \int_{\Gamma_c} |\{(\nabla v \cdot \boldsymbol{n})\boldsymbol{n}\}|^2 < \infty\right\}$, endowed with the norm $\|v\| := \left(\int_{\Gamma_c} |\{(\nabla v \cdot \boldsymbol{n})\boldsymbol{n}\}|^2 + \int_{\Omega\setminus\Gamma_c} |\nabla v|^2 + \int_\Omega |v|^2\right)^{1/2}$.

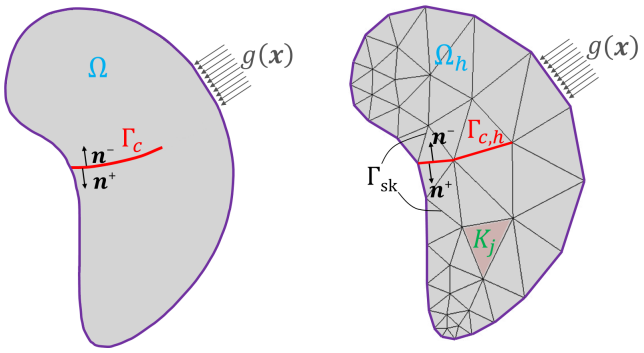

Figure 1: "Curved" (left) and "polygonal" (right) domains and interfaces.

§3. Discretization and flux formulation

We define a "polygonal" domain $\Omega_h \in \mathbb{R}^3$ and interface $\Gamma_{c,h} \subset \Omega_h$, as approximations of the "curved" domain Ω and the interface Γ_c respectively (see Figure 1). We discretize Ω_h by means of a triangulation, $\mathcal{T}_h = \{K\}$ of simplexes K, conforms to $\Gamma_{c,h}$.

We define the finite dimensional complex-valued spaces associated to $\mathcal{T}_h$

$$V_h := \{v \in L^2(\Omega_h) \mid v|_K \in \mathcal{P}_p(K),\ \forall K \in \mathcal{T}_h\},$$
$$\Sigma_h := \{\boldsymbol{\tau} \in [L^2(\Omega_h)]^3 \mid \boldsymbol{\tau}|_K \in [\mathcal{P}_p(K)]^3,\ \forall K \in \mathcal{T}_h\},$$

being $\mathcal{P}_p(K)$ the space of multivariable polynomial functions of degree $p \geq 2$.

In order to obtain the the DGFEM, we rewrite equation (1a) as a first-order system

$$\boldsymbol{\sigma} = \nabla u, \qquad \nabla \cdot \boldsymbol{\sigma} + i\frac{2\pi\nu}{\alpha} u = 0, \qquad \text{in } \Omega_h \setminus \Gamma_{c,h}. \tag{2}$$

Multiplying the first and the second equations in (2) by test functions $\boldsymbol{\tau} \in \Sigma_h$ and $v \in V_h$ respectively, integrating by using the following identity derived from the divergence theorem

$$\int_K a\, \nabla \cdot \boldsymbol{b} + \int_K \boldsymbol{b} \cdot \nabla a = \int_{\partial K} a\, \boldsymbol{b} \cdot \boldsymbol{n} \tag{3}$$

in all simplexes, we have formally

$$\begin{cases} \displaystyle\sum_{K\in\mathcal{T}_h} \int_K \boldsymbol{\sigma} \cdot \boldsymbol{\tau} = -\sum_{K\in\mathcal{T}_h} \int_K u\, \nabla \cdot \boldsymbol{\tau} + \sum_{K\in\mathcal{T}_h} \int_{\partial K} u\, \boldsymbol{n}_K \cdot \boldsymbol{\tau}, \\ \displaystyle\sum_{K\in\mathcal{T}_h} \int_K \boldsymbol{\sigma} \cdot \nabla v = \sum_{K\in\mathcal{T}_h} \int_{\partial K} \boldsymbol{\sigma} \cdot \boldsymbol{n}_K\, v + \int_{\Omega_h} i\frac{2\pi\nu}{\alpha} u\, v. \end{cases}$$

The so-called *flux formulation* is the following quite general discrete approximation of

(2): Find $u_h \in V_h$ and $\boldsymbol{\sigma_h} \in \Sigma_h$ such that

$$\begin{cases} \displaystyle\sum_{K\in\mathcal{T}_h}\int_K \boldsymbol{\sigma_h}\cdot\boldsymbol{\tau} = -\sum_{K\in\mathcal{T}_h}\int_K u_h\nabla\cdot\boldsymbol{\tau} + \sum_{K\in\mathcal{T}_h}\int_{\partial K}\hat{u}_K\boldsymbol{n}_K\cdot\boldsymbol{\tau}, \\ \displaystyle\sum_{K\in\mathcal{T}_h}\int_K \boldsymbol{\sigma_h}\cdot\nabla v = \sum_{K\in\mathcal{T}_h}\int_{\partial K}\hat{\boldsymbol{\sigma}}_{\boldsymbol{k}}\cdot\boldsymbol{n}_K v + \int_{\Omega_h} i\frac{2\pi\nu}{\alpha}u_h v, \end{cases} \tag{4}$$

being $\hat{u}_K \approx u|_{\partial K}$ and $\hat{\boldsymbol{\sigma}}_K \approx \nabla u|_{\partial K} = \boldsymbol{\sigma}|_{\partial K}$ the *numerical fluxes*.

3.1. The *primal formulation*

Following the methodology presented by Douglas *et al.* in (cf. [1]), we have to eliminate the auxiliary variable $\boldsymbol{\sigma_h}$ in equation (4) in order to obtain the so-called *primal formulation*.

Let us denote $\Gamma_{sk} = \cup_{K\in\mathcal{T}_h}\partial K \setminus (\Gamma_{c,h}\cup\partial\Omega_h)$ the interior skeleton of $\mathcal{T}_h$ (see Figure 1) and introduce the space of functions on Ω_h, $H^1(\mathcal{T}_h)$, whose restrictions to each element K belongs to the Sobolev space $H^1(K)$.

By using the identity

$$\sum_{K\in\mathcal{T}_h}\int_{\partial K} a_K\boldsymbol{b_K}\cdot\boldsymbol{n}_K = \int_{\Gamma_{sk}\cup\Gamma_{c,h}}[\![a]\!]\cdot\{\boldsymbol{b}\} + \int_{\Gamma_{sk}\cup\Gamma_{c,h}}\{a\}\,[\![\boldsymbol{b}]\!] + \int_{\partial\Omega_h} a\,\boldsymbol{n}\cdot\boldsymbol{b}, \tag{5}$$

for all $a \in H^1(\mathcal{T}_h)$ and all $\boldsymbol{b} \in [H^1(\mathcal{T}_h)]^3$, we can rewrite the *flux formulation* (4) as follows:

$$\begin{cases} \displaystyle\sum_{K\in\mathcal{T}_h}\int_K \boldsymbol{\sigma_h}\cdot\boldsymbol{\tau} = -\sum_{K\in\mathcal{T}_h}\int_K u_h\nabla\cdot\boldsymbol{\tau} + \int_{\Gamma_{sk}\cup\Gamma_{c,h}}([\![\hat{u}]\!]\cdot\{\boldsymbol{\tau}\} + \{\hat{u}\}[\![\boldsymbol{\tau}]\!]) + \int_{\partial\Omega_h}\hat{u}\,\boldsymbol{n}\cdot\boldsymbol{\tau} \\ \displaystyle\sum_{K\in\mathcal{T}_h}\int_K \boldsymbol{\sigma_h}\cdot\nabla v = \int_{\Gamma_{sk}\cup\Gamma_{c,h}}([\![v]\!]\cdot\{\hat{\boldsymbol{\sigma}}\} + \{v\}[\![\hat{\boldsymbol{\sigma}}]\!]) + \int_{\partial\Omega_h} v\,\boldsymbol{n}\cdot\hat{\boldsymbol{\sigma}} + \int_{\Omega_h} i\frac{2\pi\nu}{\alpha}u_h v \end{cases} \tag{6}$$

Furthermore, applying identities (3) and (5) we have that for $u_h \in V_h$ and $\boldsymbol{\tau} \in \Sigma_h$

$$-\int_{\mathcal{T}_h} u_h\nabla\cdot\boldsymbol{\tau} = \int_{\mathcal{T}_h}\nabla u_h\cdot\boldsymbol{\tau} - \int_{\Gamma_{sk}\cup\Gamma_{c,h}}([\![u_h]\!]\cdot\{\boldsymbol{\tau}\} + \{u_h\}[\![\boldsymbol{\tau}]\!]) - \int_{\partial\Omega_h} u_h\boldsymbol{n}\cdot\boldsymbol{\tau}. \tag{7}$$

Substituting the equality (7) in the first equation of (6) and taking $\boldsymbol{\tau} = \nabla v$, we get

$$\begin{cases} \displaystyle\sum_{K\in\mathcal{T}_h}\int_K \boldsymbol{\sigma_h}\cdot\nabla v = \sum_{K\in\mathcal{T}_h}\int_K\nabla u_h\cdot\nabla v + \int_{\Gamma_{sk}\cup\Gamma_{c,h}}([\![\hat{u}-u_h]\!]\cdot\{\nabla v\} + \{\hat{u}-u_h\}[\![\nabla v]\!]) \\ \qquad\qquad + \displaystyle\int_{\partial\Omega_h}(\hat{u}-u_h)\boldsymbol{n}\cdot\nabla v, \\ \displaystyle\sum_{K\in\mathcal{T}_h}\int_K \boldsymbol{\sigma_h}\cdot\nabla v = \int_{\Gamma_{sk}\cup\Gamma_{c,h}}([\![v]\!]\cdot\{\hat{\boldsymbol{\sigma}}\} + \{v\}[\![\hat{\boldsymbol{\sigma}}]\!]) + \int_{\partial\Omega_h} v\boldsymbol{n}\cdot\hat{\boldsymbol{\sigma}} + \int_{\Omega_h} i\frac{2\pi\nu}{\alpha}u_h v. \end{cases} \tag{8}$$

By subtraction in (8) and reorganizing terms, we obtain the so called *primal formulation*:

$$\begin{aligned} \sum_{K\in\mathcal{T}_h}\int_K\nabla u_h\cdot\nabla v - \int_{\Omega_h} i\frac{2\pi\nu}{\alpha}u_h v + \int_{\Gamma_{sk}\cup\Gamma_{c,h}}([\![\hat{u}-u_h]\!]\cdot\{\nabla v\} + \{\hat{u}-u_h\}[\![\nabla v]\!] - [\![v]\!]\cdot\{\hat{\boldsymbol{\sigma}}\} - \{v\}[\![\hat{\boldsymbol{\sigma}}]\!]) \\ + \int_{\partial\Omega_h}((\hat{u}-u_h)\boldsymbol{n}\cdot\nabla v - v\,\boldsymbol{n}\cdot\hat{\boldsymbol{\sigma}}) = 0. \end{aligned} \tag{9}$$

3.2. Choices of the numerical fluxes

The particular type of DG method that we apply is defined by the choice of the following numerical fluxes:

1. On the skeleton, Γ_{sk}, we chose the same numerical fluxes as in Baumann-Oden DGFEM:

$$\begin{cases} \hat{u}\big|_{\Gamma_{sk}} = \{u_h\} + \boldsymbol{n}_K[\![u_h]\!], \\ \hat{\boldsymbol{\sigma}}\big|_{\Gamma_{sk}} = \{(\nabla u_h \cdot \boldsymbol{n})\boldsymbol{n}\}. \end{cases}$$

2. On the interface, $\Gamma_{c,h}$, where the crack is placed the choice of the numerical fluxes are:

$$\begin{cases} \hat{u}\big|_{\Gamma_{c,h}} = \{u_h\} + \dfrac{1}{2}\boldsymbol{n}_K[\![u_h]\!] + \dfrac{1}{2}\dfrac{h_e}{h_e + c\kappa R^2}\boldsymbol{n}_K([\![u_h]\!] + \kappa R\{\nabla u_h\} - \boldsymbol{f_2}), \\ \hat{\boldsymbol{\sigma}}\big|_{\Gamma_{c,h}} = \{(\nabla u_h \cdot \boldsymbol{n})\boldsymbol{n}\} + \dfrac{1}{2}\boldsymbol{n}_K \cdot [\![\nabla u_h]\!] \\ \qquad\qquad = \dfrac{h_e}{h_e + c\kappa R^2}(\nabla u_h \cdot \boldsymbol{n})\boldsymbol{n} + \dfrac{cR}{h_e + c\kappa R^2}(\boldsymbol{f_2} - [\![u_h]\!]) + \dfrac{1}{2}\boldsymbol{n}_K f_1, \end{cases}$$

   being h_e the average of the diameters of the smallest circumscribed sphere around of each simplex that share a face, and where $c \in \mathbb{R}$ is a constant with dimensions of $[P][L]^{-2}[T]^{-1}$ that gives us a robust family of DG methods depending on the value of the constant.

3. On the boundary $\partial\Omega_h$ the fluxes are: $\hat{u}\big|_{\partial\Omega_h} = u_h|_{\partial\Omega_h}$ and $\hat{\boldsymbol{\sigma}}\big|_{\partial\Omega_h} = \frac{g}{\kappa}\boldsymbol{n}$.

3.3. The variational form

Substituting the numerical fluxes in the *primal formulation* (9) and reordering, we get the following c-parameter dependent family of variational forms: Find $u_h \in V_h$ such that

$$\begin{aligned} &\sum_{K\in\mathcal{T}_h}\int_K \nabla u_h \cdot \nabla v - \int_{\Omega_h} i\frac{2\pi\nu}{\alpha}u_h v + \int_{\Gamma_{sk}} [\![u_h]\!]\cdot\{\nabla v\} - \int_{\Gamma_{sk}} [\![v]\!]\cdot\{\nabla u_h\} + \int_{\Gamma_{c,h}} \frac{h_e}{h_e + c\kappa R^2}[\![u_h]\!]\cdot\{\nabla v\} \\ &- \int_{\Gamma_{c,h}} \frac{h_e}{h_e + c\kappa R^2}\{\nabla u_h\}\cdot[\![v]\!] + \int_{\Gamma_{c,h}} \frac{h_e\kappa R}{h_e + c\kappa R^2}\{\nabla u_h\cdot\boldsymbol{n}\}\{\nabla v\cdot\boldsymbol{n}\} + \int_{\Gamma_{c,h}} \frac{cR}{h_e + c\kappa R^2}[\![u_h]\!]\cdot[\![v]\!] \\ &= \int_{\Gamma_{c,h}} \frac{h_e}{h_e + c\kappa R^2}\boldsymbol{f_2}\cdot\{\nabla v\} + \int_{\Gamma_{c,h}} \frac{cR}{h_e + c\kappa R^2}\boldsymbol{f_2}\cdot[\![v]\!] + \int_{\Gamma_{c,h}} \frac{f_1}{\kappa}\{v\} + \frac{1}{\kappa}\int_{\partial\Omega_h} gv, \quad \forall v \in V_h. \end{aligned} \tag{10}$$

For sake of simplicity and rapidness we can choose $c = 0$ that let us becoming the variational form (10) much more simple:

$$\begin{aligned} &\sum_{K\in\mathcal{T}_h}\int_K \nabla u_h \cdot \nabla v - \int_{\Omega_h} i\frac{2\pi\nu}{\alpha}u_h v + \int_{\Gamma_{sk}} [\![u_h]\!]\cdot\{\nabla v\} - \int_{\Gamma_{sk}} [\![v]\!]\cdot\{\nabla u_h\} + \int_{\Gamma_{c,h}} [\![u_h]\!]\cdot\{\nabla v\} \\ &- \int_{\Gamma_{c,h}} \{\nabla u_h\}\cdot[\![v]\!] + \int_{\Gamma_{c,h}} \kappa R\{\nabla u_h\cdot\boldsymbol{n}\}\{\nabla v\cdot\boldsymbol{n}\} = \frac{1}{\kappa}\int_{\partial\Omega_h} gv + \int_{\Gamma_{c,h}} \boldsymbol{f_2}\cdot\{\nabla v\} + \int_{\Gamma_{c,h}} \frac{f_1}{\kappa}\{v\}. \end{aligned} \tag{11}$$

§4. Numerical results

In order to illustrate how DGFEM works and to estimate its order of convergence, we perform some numerical experiments in a normalized 1D problem (P) of (1), with $\Omega \equiv \Omega_h = (0, 4\mu)$, being $\mu = \sqrt{\frac{\alpha}{\pi\nu}}$ the thermal-diffusion length, $\Gamma_c = \{2\mu\}$, $g(0) = -\kappa/\mu$, $f_1 = 0$, $\boldsymbol{f_2} = 0$. The exact solution of (P), with $R = \mu/\kappa$, is $u(\cdot) = \tilde{u}(\frac{\cdot}{\mu})$, being $\tilde{u}(x) = c_1 e^{-x+ix} + c_2 e^{x-ix}$ for $x \in [0, 2)$ and $\tilde{u}(x) = c_3 e^{-x+ix} + c_4 e^{x-ix}$ for $x \in (2, 4]$, where $c_1 = \frac{(1+i)e^{-4+i4} - 1 - 3i}{2ie^{-8+i8} + 4e^{-4+i4} - 4 - 2i}$, $c_2 = c_1 - (1+i)/2$, $c_3 = \frac{-1}{e^{-8+i8} - 2ie^{-4+i4} - 1 + 2i}$ and $c_4 = c_3 e^{-8+i8}$. For the numerical approximation we solve the variational formulation (11) in an uniform mesh with $h = \mu/2$ and $p = 2$. In Figure 2 we show both exact and numerical solutions of (P) with $R = \mu/\kappa$. It can be observed the discontinuity of the exact solutions u, the continuity of its lateral gradients ($\nabla u(x^-) = \nabla u(x^+)$ for $x \in \Omega$) and the jumps $[\![u_h]\!]$ and $[\![\nabla u_h]\!]$ in the interface $\Gamma_c \equiv \Gamma_{c,h}$ and in the skeleton $\Gamma_{sk} = \{k\frac{\mu}{2} \mid k = 1, 2, 3, 5, 6, 7\}$ of the approximate solution.

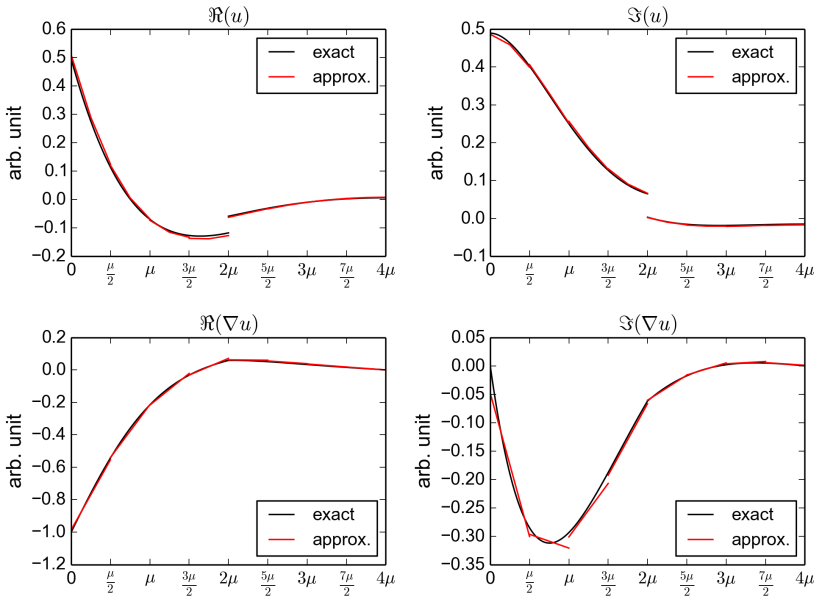

Figure 2: Representation in $\Omega \setminus \{\Gamma_c \cup \Gamma_{sk}\}$ of the exact and numerical solutions of the normalized problem (P) with thermal contact resistance $R = \mu/\kappa$.

We estimate the quantitative approximation error, $u_h - u$, in the H^1-type norm

$$|||v|||^2 = \sum_{K\in\mathcal{T}_h} \int_K |\nabla v|^2 + \sum_{\partial K\in\Gamma_{sk}} \frac{1}{h} \int_{\partial K} |[\![v]\!]|^2 + \sum_{\partial K\in\partial\Omega} \int_{\partial K} |v|^2$$
$$+ \sum_{\partial K\in\Gamma_c} \int_{\partial K} \left(\frac{1}{\kappa R + h} |[\![v]\!]|^2 + |\{(\nabla v \cdot \boldsymbol{n})\boldsymbol{n}\}|^2 \right), \qquad \text{for all } v \in V + V_h,$$

with the convention in the 1D case $\int_{\partial K} w := w|_{\partial K}$, for all $\partial K \in \Gamma_c \bigcup \Gamma_{sk} \bigcup \partial\Omega$.

In Table 1 we show values of the error $|||u_h - u|||$ in uniform meshes of the numerical approximation (11) of problem (P) with $R = \mu/\kappa$, and the estimate order of convergence,

$$\text{EoC} = \frac{\log\left(\, |||u_{h_1} - u|||/|||u_{h_1/2} - u|||\right)}{\log 2}.$$

h	$\mu/2$	$\mu/4$	$\mu/8$	$\mu/16$	$\mu/32$	$\mu/64$	$\mu/128$
$\|\|\|u_h - u\|\|\|$	3.16865974e-02	1.02190775e-02	2.93616848e-03	7.88965573e-04	2.04593375e-04	5.20981435e-05	1.31451663e-05
EoC	—	1.63260778	1.7992583	1.8959005	1.94720292	1.97345556	1.98669957

Table 1: Errors and EoCs of the normalized problem (P) with $R = \mu/\kappa$.

The estimated order of convergence goes to 2, the same as the degree p of the polynomial chosen in the DGFEM. This estimation is agree with the results of convergence in a weaker norm related to the Baumann-Oden method for the Poisson equation with homogeneous Dirichlet boundary conditions analyzed in (cf. [13]).

In Figure 3 we can see the uniform behavior of the relative error in function of R for the approximation solution of problem (P). The relative error tends to be divided by four when doubling the number of elements in uniform meshes. Assuming uniform converge of order 2 for $R \geq 0$, we can derive the following pointwise convergence result for the jump on the crack: exist $C > 0$ independent of h and R such that $\left|[\![u]\!]_{\Gamma_c} - [\![u_h]\!]_{\Gamma_c}\right| \leq Ch^2\sqrt{\kappa R + h}\,|||u|||$.

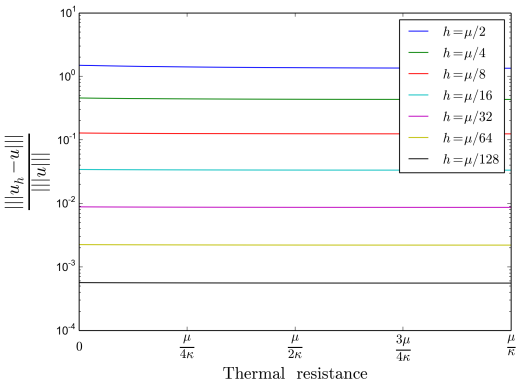

Figure 3: Behavior of the relative error for different R and discretizations of problem (P)

Let us remark that hybridizable DG methods (see cf. [7], [6] and references therein) are more efficient than the Baumann-Oden-type method here exposed, but unlikely they have not yet been implemented in FEniCS (cf. [11]), the collection of free software we using for our practical purposes in active thermography simulations.

§5. Photothermal application

Let us consider a cracked gear made of AISI-E9310 alloy steel with $\kappa = 51.9 Wm^{-1}K^{-1}$ and $\alpha = 1.4E^{-5}m^2s^{-1}$ (cf. [12]). Although is know that thermophysical properties of hardened gears are function of depth (cf. [3]) for simplicity, we do not take this into account.

We model a lock-in thermographic inspection ($f_1 = 0$, $\boldsymbol{f_2} = 0$) where the exciting laser spot (see Figure 4) at frequency $\nu = 1Hz$ is modeled by a Gaussian function $g(\boldsymbol{x}) = \frac{2I_o}{\pi a^2} e^{-\frac{2}{a^2}\|\boldsymbol{x}-\boldsymbol{x_c}\|}$ with radius $a = 0.5mm$; the center of the laser spot is placed at point $\boldsymbol{x_c} = (0, -2.5, 0)$, units in mm. The interface related to a rectangular crack, vertical to the upper surface $x_3 = 0$, is $112.163\mu m$ long, $3mm$ deep (axe Z), and it is upper vertices are $(-0.257819, -3.42122, 0)$ and $(-0.145656, -3.42122, 0)$. The effective thickness or the crack is $R\kappa_{air} = 2.6\mu m$, being $\kappa_{air} = 0.026 Wm^{-1}K^{-1}$.

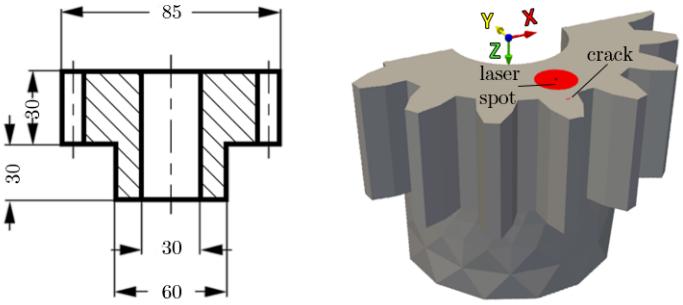

Figure 4: Dimensions of the gear (expressed in mm) with number of teeth $z = 15$ and module $m = 5$ (left). 3D scheme of the gear (right), the axes are placed at the origin.

In order to solve the variational form (11) we choose the finite element family of three dimensional complex-valued discontinuous Lagrange elements of degree 2. Due to complex numbers are not supported in the software used for the implementation, we have to uncouple in real and imaginary part and we have to define a mixed function spaces that are created by taking the product of simpler spaces of three dimensional discontinuous Lagrange of degree 2. Therefore we have 20 real unknowns for each tetrahedron.

We present some results of the numerical simulation that has been implemented by using a collection of scientific open-source software, NETGEN as mesh generator, FEniCS (cf. [11]) for automated solution of differential equations by FEM and for data visualization Matplotlib plotting library and ParaView. In Figure 5 we can see the solutions of the real and imaginary part of the temperature on the illuminated surface of the gear. In Figure 6 we present a detail of the cracked teeth where we can show the logarithm of the temperature amplitude and phase. We can see the jump along the crack remarked by the blue profile and the continuity of the profile represented by the green line placed out of the crack.

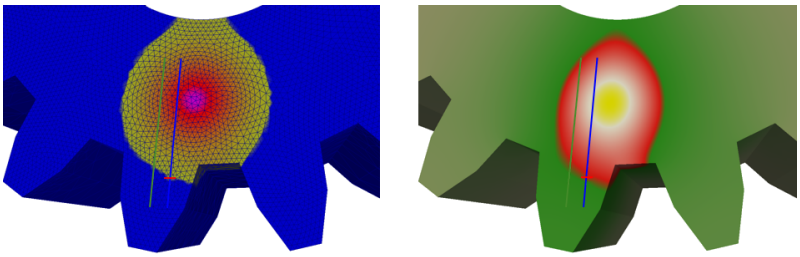

Figure 5: Real (left) and imaginary (right) part of the numerical solution of the temperature obtained on the gear surface. The red line represents the crack.

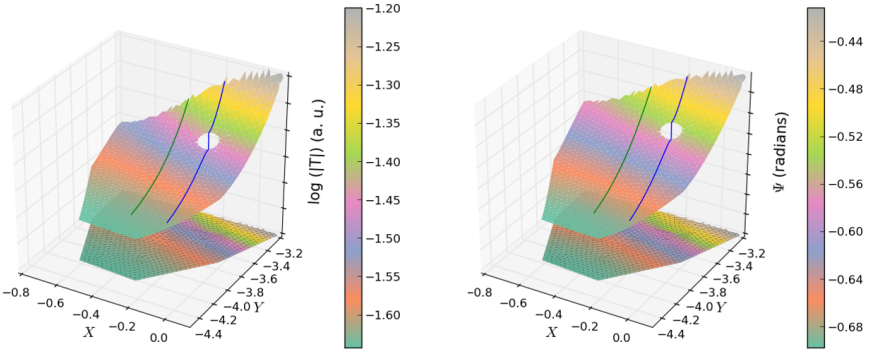

Figure 6: Detail of the superficial temperature $T = |T|e^{i\Psi}$, logarithm of amplitude (left) and phase (right), on the illuminated surface of the teeth with crack.

Acknowledgements

This work has been supported by the Spanish government projects ref. MTM2013-40842-P and MAT2011-23811 and by the Diputación General de Aragón (Grupo consolidado PDIE). Omella gratefully acknowledge to the organization of the XIII International Conference Zaragoza-Pau on Mathematics and its Applications.

References

[1] Arnold, D. N., Brezzi, F., Cockburn, B., and Marini, L. D. Unified analysis of discontinuous galerkin methods for elliptic problems. *SIAM J. Numer. Anal. 39* (2001), 1749–1779.

[2] Breitenstein, O., Warta, W., and Langenkamp, M. *Lock-in thermography: Basics and use for evaluating electronic devices and materials*. Springer, 2010.

[3] Celorrio, R., Apiñaniz, E., Mendioroz, A., Salazar, A., and Mandelis, A. Accurate reconstruction of the thermal conductivity depth profile in case hardened steel. *Journal of Applied Physics 107* (2010).

[4] Celorrio, R., Omella, A. J., Mendioroz, A., Oleaga, A., and Salazar, A. Advances in crack characterization by lock-in infrared thermography. *International Journal of Thermophysics* (2014), 1–6.

[5] Celorrio, R., Omella, A. J., Pech-May, N. W., Oleaga, A., Mendioroz, A., and Salazar, A. Vertical cracks characterization using lock-in thermography: II finite cracks. *Measurement Science and Technology 25* (2014), 115602.

[6] Cockburn, B., Gopalakrishnan, J., and Lazarov, R. Unified hybridization of discontinuous galerkin, mixed, and continuous galerkin methods for second order elliptic problems. *SIAM Journal on Numerical Analysis 47* (2009), 1319–1365.

[7] Cockburn, B., Gopalakrishnan, J., and Sayas, F.-J. A projection-based error analysis of hdg methods. *Mathematics of Computation 79* (2010), 1351–1367.

[8] Johnson, C. *Numerical Solution of Partial Differential Equations by the Finite Element Method*. Cambridge U. Press, 1987.

[9] Kubiak, E. J. Infrared detection of fatigue cracks and other near-surface defects. *Appl. Opt. 7* (1968), 1743–1747.

[10] Li, T., Darryl, Almond, D. P., and Rees, D. A. S. Crack imaging by scanning laser-line thermography and laser-spot thermography. *Measurement Science and Technology 22* (2011).

[11] Logg, A., Mardal, K.-A., Wells, G. N., et al. *Automated Solution of Differential Equations by the Finite Element Method*. Springer, 2012.

[12] MatWeb-LLC. Matweb material property data [online]. 2011. Available from: `http://www.matweb.com/` [cited November 2014].

[13] Oden, J. T., Babuska, I., and Baumann, C. E. A discontinuous hp finite element method for diffusion problems. *Journal of Computational Physics 146* (1998), 491 – 519.

[14] Schlichting, J., Maierhofer, C., and Kreutzbruck, M. Crack sizing by laser excited thermography. *NDT&E International 45* (2012), 133 – 140.

[15] Streza, M., Fedala, Y., Roger, J. P., Tessier, G., and Boue, C. Heat transfer modeling for surface crack depth evaluation. *Measurement Science and Technology 24*, 045602.

[16] Wu, D., and Busse, G. Lock-in thermography for nondestructive evaluation of materials. *Revue Generale de Thermique 37* (1998), 693–703.

A. J. Omella and R. Celorrio
Departamento de Matemática Aplicada, EINA/IUMA, Universidad de Zaragoza.
Campus Río Ebro, Edificio Torres Quevedo, 50018 Zaragoza, Spain.
`ajaome@unizar.es` and `celorrio@unizar.es`